Yang, L., Malki, M., Muñoz Ferreras, J.M. & Gómez García, R. 2022, "Balanced quasi-elliptic-type dual-passband filters using planar transversal coupled-line sections and their digital modeling", International Journal of Microwave and Wireless Technologies, DOI: 10.1017/s175907872200071X.

(Article begins on next page)

International Journal of Microwave and Wireless Technologies

cambridge.org/mrf

Research Paper

Cite this article: Yang L, Malki M, Muñoz-Ferreras J-M, Gómez-García R (2022). Balanced quasi-elliptic-type dual-passband filters using planar transversal coupled-line sections and their digital modeling. *International Journal of Microwave and Wireless Technologies* 1–10. https://doi.org/10.1017/S175907872200071X

Received: 14 April 2022
Revised: 27 May 2022
Accepted: 29 May 2022

Key words:
Balanced filter; bandpass filter (BPF); dual-band filter; microstrip filter; parallel coupled line; planar filter; signal-interference filter; transmission zero (TZ); transversal section

Author for correspondence:
Roberto Gómez-García, E-mail: roberto.gomez.garcia@ieee.org

Balanced quasi-elliptic-type dual-passband filters using planar transversal coupled-line sections and their digital modeling

Li Yang, Mohamed Malki, José-María Muñoz-Ferreras and Roberto Gómez-García

Department of Signal Theory and Communications, University of Alcalá, Alcalá de Henares 28871, Madrid, Spain

Abstract

A class of balanced dual-band bandpass filters (BPFs) with planar transversal-signal-interference coupled-line sections is reported. In their building balanced dual-band BPF stage under differential-mode excitation, a second-order quasi-elliptic-type dual-band bandpass filtering transfer function is obtained. Specifically, from the transversal interaction among their two open-ended and virtually-short-ended half-wavelength coupled-line paths, sharp-rejection differential-mode dual passbands with several out-of-band transmission zeros at both sides are realized. To attain high common-mode suppression levels within the differential-mode passbands, two open-ended line segments are connected at the symmetry plane of the devised balanced dual-band BPF stage. Moreover, higher-order schemes based on in-series-cascaded multi-stage designs to further increase differential-mode selectivity and in-band common-mode rejection are illustrated. The operational principles and parametric-analysis design rules of the engineered transversal-coupled-line-based balanced dual-band BPF approach are detailed. Additionally, for a rigorous interpretation of their zero/pole characteristics, a digital-modeling framework is applied to them to connect RF balanced filters with their discrete-time versions. For practical-validation purposes, a microstrip prototype of two-stage/fourth-order balanced dual-band BPF is built and tested. It exhibits measured differential-mode dual passbands with center frequencies of 1.464 and 2.294 GHz, 3 dB fractional bandwidths of 8.74 and 9.68%, and in-band common-mode rejection levels above 23.16 and 31.36 dB, respectively.

Introduction

In order to meet the ever-stringent demands of emerging wireless-communication systems, RF microwave components with various enhanced functionalities are always desired. Among them, a plurality of research activities aimed at developing balanced/differential-mode bandpass filters (BPFs) with multi-band bandpass transfer functions are recently attracting considerable attention [1]. Such RF multi-band pre-selection devices are expected to be required by modern multi-standard/multi-purpose highly-integrated RF front-end chains. This is because they are more robust than their single-ended counterparts to undesired common-mode noise and electromagnetic (EM)-interference/crosstalk effects that may arise between the different layers in ultra-compact/highly-miniaturized RF transceivers as on-going RF system-level design trend.

When compared to balanced single-band BPFs, it becomes more difficult to design differential-mode dual- or multi-band BPFs with satisfactory common-mode-rejection performance. In order to achieve high common-mode suppression levels within the differential-mode passbands, balanced dual-/multi-band BPFs using different design techniques have been reported in the technical literature as in [2–11]. They mostly consist of coupled-resonator filter configurations that are properly modified to attain the differential-mode dual-passband filtering behavior while simultaneously suppressing the in-band common-mode RF signal. For example, by exploiting asymmetrical or symmetrical open-ended stubs loaded at the filter symmetry plane, balanced dual-band BPFs using coupled stepped-impedance resonators (SIRs) [2], doubly short-ended coupled lines [3], SIR ring resonators [4], and stub-loaded shunted-line resonators [5] were studied. In [6], balanced dual-band BPFs with asymmetrical SIR-based coupled lines were developed. Subsequently, by using four U-shaped slotline resonators etched at the ground plane, a type of compact balanced dual-band BPF using coupled-embedded SIR resonators was presented in [7]. In yet another approach, by making use of the intrinsic common-mode-rejection property of balanced microstrip-to-slotline transitions, differential-mode multi-band and dual-band BPFs realized in four-port balanced topologies were discussed in [8] and [9], respectively. Moreover, based on a four-port wideband balanced branch-line structure loaded with two pairs of multiple short-circuit-ended stubs, a class of differential-mode planar multi-band BPFs was engineered in [10]. Similarly, balanced dual-band BPFs with symmetrical quasi-reflectionless behavior can also be developed, as it was corroborated in [11]. However, most of the aforementioned balanced dual-/multi-band BPF architectures suffer from some drawbacks, such as relatively-poor selectivity around the differential-mode passbands, among some others.

On the other hand, transversal-signal-interference RF passive filters have emerged in the last few years as a suitable alternative to coupled-resonator circuit networks for single/multi-band BPF design using non-conventional multi-path filtering structures [12–17]. Examples of their employed constituent transversal filtering sections include bi-path in-parallel-transmission-line-based cells and directional power couplers and dividers with loaded stubs, which are arranged in transversal mode. In this manner, from the frequency-dependent constructive/destructive interference phenomena at the output node among the multiple signal components in which the input signal is divided to produce passbands/stopbands, single/multi-band BPFs with ultra-sharp rejection capabilities can be generated. Nevertheless, due to their intrinsic frequency-periodic behavior in most cases, and more especially for multi-band BPFs, they suffer from narrow stopband bandwidths [15]. Whereas the exploitation of stepped-impedance-line paths in transversal signal-interference dual-band BPFs has been recently proposed in [18] as an effective technique to partially circumvent this limitation, the problem still remains at the lower stopband. Furthermore, it should be remarked upon that most of these transversal-signal-interference filters are of the single-ended type, with just a very few cases of differential-mode multi-band BPFs that heritage the referred drawback from their single-ended precursors as the one simulated in [19] that lacks from experimental demonstration.

In this paper, as an extension of the preliminary work from the authors in [20] for the single-ended case, an original type of balanced quasi-elliptic-type dual-band BPFs is developed. In differential-mode operation, they exploit as basic building block a two-path coupled-line-based transversal filtering section in which a second-order sharp-rejection dual-band BPF response with several close-to-passband transmission zeros (TZs) at both passband sides is obtained. When compared to their transversal single-ended and balanced dual-band BPF precursors without coupled-line stages in their circuit networks, enlarged stopband bandwidths are attained. Furthermore, by properly adjusting the line-impedance values of the open-ended stubs that are loaded at the filter symmetry plane, high common-mode rejection levels within the differential-mode passbands can be achieved through in-band common-mode multi-TZ generation. Higher-order realizations composed of in-series cascade connections of several replicas of the balanced dual-band BPF stage are also feasible, as theoretically verified with a fourth-order two-stage design example. In addition, the discrete-time modeling of the reported balanced dual-band BPFs is also presented toward a better understanding of its zero/pole characteristics. Note that although this framework was previously applied to single-ended transversal-signal-interference and coupled-line filters in [21] and [22], respectively, this is the first time that this modeling technique is extended to differential-mode RF filters, hence allowing to “mimic” their behavior from a digital perspective. Finally, for experimental-demonstration purposes, a 1.464/2.294 GHz proof-of-concept microstrip prototype of the designed two-stage/fourth-order differential-mode dual-band BPF example is manufactured and characterized.

Design, analysis, and digital modeling

This section presents the RF operational principles of the proposed transversal-signal-interference coupled-line-based balanced dual-band BPF. First, the theoretical foundations of its constituent second-order differential-mode dual-band BPF stage and design guidelines based on parametric-circuit analysis are reported. Subsequently, the feasibility of higher-order in-series-cascaded multi-stage designs to attain increased differential-mode selectivity and higher in-band common-mode suppression levels is demonstrated in a two-stage/fourth-order balanced dual-band BPF realization. Finally, as a further original contribution of this work related with the modeling of balanced dual-band BPFs in the digital domain – which is demonstrated here by the very first time for balanced RF filters – the discrete-time representation of single-stage/second-order and two-stage/fourth-order theoretical design examples is addressed.

Second-order balanced dual-band BPF

The equivalent circuit of the proposed second-order balanced dual-band BPF stage with indication of its design parameters is depicted in Fig. 1(a). The properties of this balanced circuit are determined by means of its associated two-port differential- and common-mode equivalent sub-circuits, respectively. When the differential-mode RF signals are excited at the pairs of input (Ports 1 and 1′) and output (Ports 2 and 2′) ports, a virtual electrical wall is produced at the symmetry plane of the balanced BPF architecture. As illustrated in Fig. 1(b), its two-port differential-mode equivalent sub-circuit is derived, in which all the circuit points that are connected to the symmetry plane become virtually short ended. Here, the open- and short-ended half-wavelength resonators are in-parallel coupled with the input and output T-junctions. In this manner, based on these four constituent coupled-line sections in the engineered two-path transversal-signal-interference section, a second-order dual-band BPF filtering response with sharp-rejection selectivity can be obtained. At the same time, the other two quarter-wavelength line segments are utilized to improve the in-band power-matching levels of the two designed passbands. On the other hand, Fig. 1(c) depicts the two-port common-mode equivalent sub-circuit of this second-order balanced BPF. A magnetic wall is then created at the symmetry plane when a common-mode excitation is applied to the pairs of input and output ports, which results in the impedance value of the loaded open-ended stubs to be doubled as $2Z_L$.

To verify the above descriptions for the proposed second-order balanced dual-band BPF, its theoretical frequency responses based on the relevant even- and odd-mode theoretical analysis of the two-port differential- and common-mode equivalent sub-circuits can be determined. Due to their mathematical complexity, these formulas have been omitted here. Various illustrative responses based on parametric-circuit analysis are provided instead as more useful information for the designer. Specifically, in Fig. 2, the theoretical power transmission and reflection responses for a design example of second-order balanced dual-band BPF under differential- and common-mode operation are presented. As can be seen, two sharp-rejection passbands with several close-to-passband TZs at their both sides are attained for the differential mode, which are spectrally symmetrical with regard to the inter-passband TZ produced at the design frequency f_0. Furthermore, by means of the selected values for the impedance-line design parameters (Z_C, Z_{0o1}, Z_{0e1}, Z_{0o2}, Z_{0e2}, and Z_L),

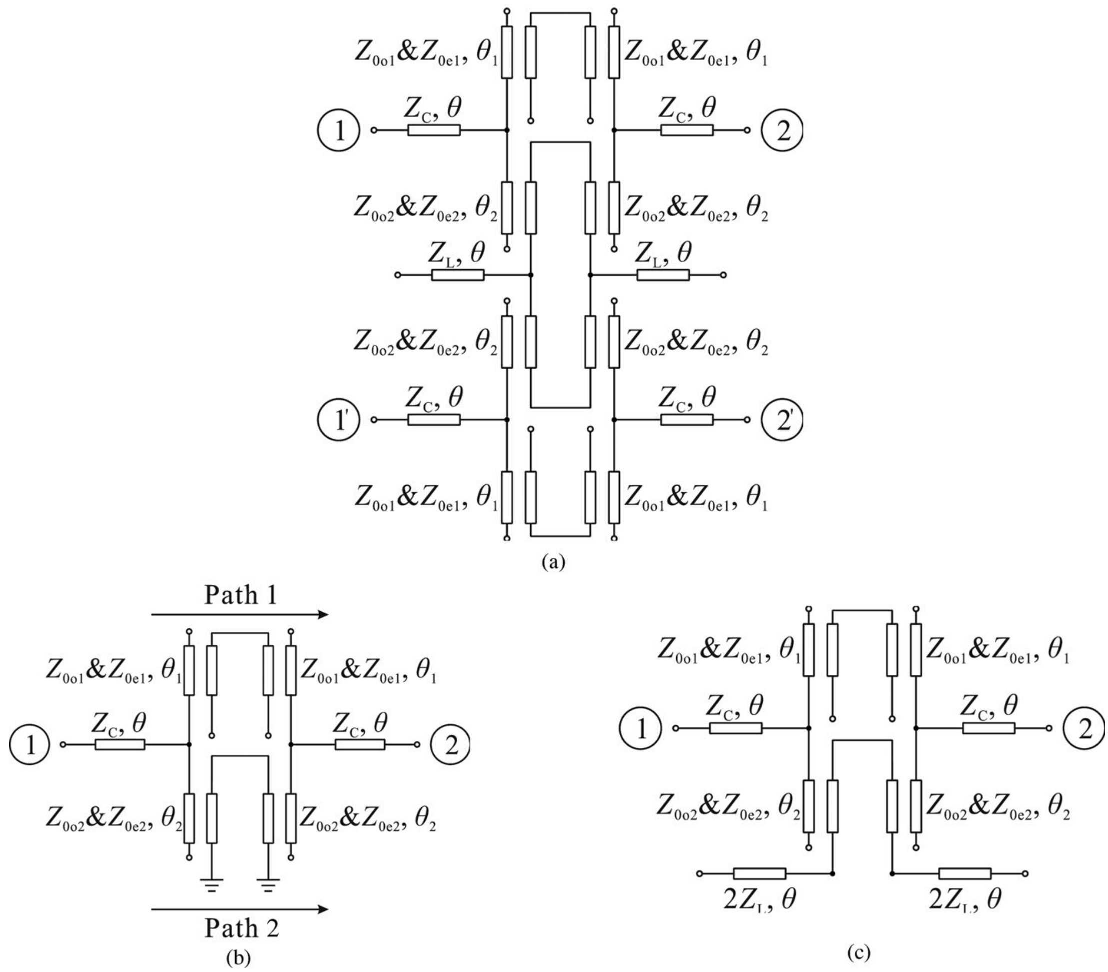

Fig. 1. Equivalent circuits of the proposed second-order balanced dual-band BPF based on a transversal-signal-interference coupled-line section. (a) Four-port balanced network with circuit detail (Z_C, Z_L, Z_{0o1}, Z_{0e1}, Z_{0o2}, and Z_{0e2} correspond to characteristic-, odd-mode-, and even-mode-impedance variables of the in-series input/output connecting lines, the shunt open-ended stubs that are loaded at the symmetry plane, and the two relevant coupled-line sections, respectively, whereas the electrical lengths θ, θ_1, and θ_2 correspond to line segments that are quarter-wavelength long at the design frequency f_0 or $\theta(f_0) = \theta_1(f_0) = \theta_2(f_0) = 90°$. (b) Two-port differential-mode equivalent sub-circuit. (c) Two-port common-mode equivalent sub-circuit.

common-mode power-rejection levels above 23.5 dB for the proposed second-order balanced BPF are attained through the generation of several common-mode multi-TZ creation within the

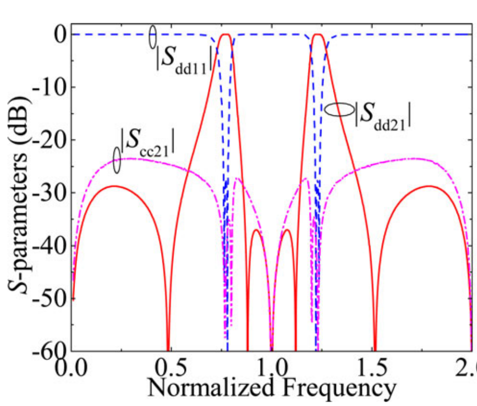

Fig. 2. Theoretical differential-mode power transmission ($|S_{dd21}|$), reflection ($|S_{dd11}|$), and common-mode suppression ($|S_{cc21}|$) responses of the proposed second-order balanced dual-band BPF in Fig. 1(a) with $Z_C = 42\Omega$, $Z_{0e1} = 77.5\Omega$, $Z_{0o1} = 31.8\Omega$, $Z_{0e2} = 98.7\Omega$, $Z_{0o2} = 32.5\Omega$, $Z_L = 16.7\Omega$, and $\theta(f_0) = \theta_1(f_0) = \theta_2(f_0) = 90°$ (reference impedance $Z_0 = 50\Omega$).

spectral period [0, $2f_0$]. Note that the TZs at DC and $2f_0$ are due to the fact of not having direct signal-transmission path (i.e. without coupled-line stages) between the input and output terminals for both the differential- and common-mode equivalent sub-networks in Figs 1(b) and 1(c), respectively. The TZ at f_0 is produced by the quarter-wavelength-at-f_0 open-ended stubs of the coupled-line stages connected to the input/output Z_C-impedance lines. The remaining TZs are caused by the transversal interaction among the two signal-propagation paths, so that the two signal components propagated by them inter-cancel out at the output node for these frequencies to produce signal transmission nulls.

To further demonstrate the design flexibility of the proposed second-order differential-mode dual-band BPF stage in Fig. 1(b) in differential-mode operation, several frequency responses with flexible dual passbands are discussed for two situations, as follows: (i) constant absolute bandwidths but different center frequencies and (ii) different absolute bandwidths but fixed TZs at the inter-passband region. Specifically, as observed in Fig. 3(a) for the selected set of values of the design impedances, quasi-elliptic-type dual passbands with constant absolute bandwidth of 77 MHz for each passband at the center frequencies of $0.7655f_0$ and $1.2345f_0$ (case 1) and $0.6715f_0$ and $1.3285f_0$ in (case 2), respectively, are

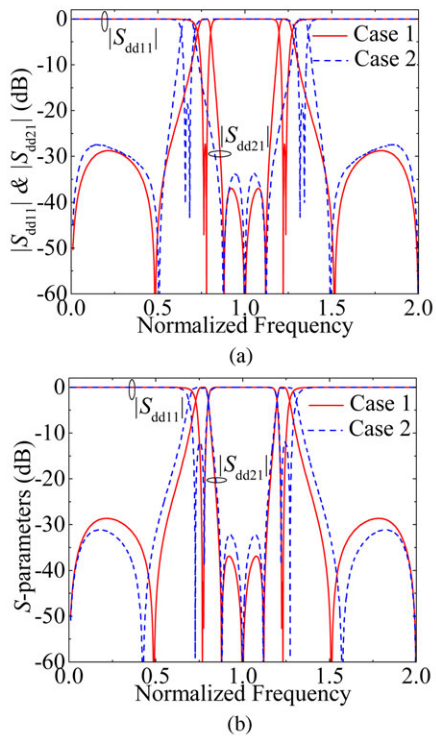

Fig. 3. Theoretical frequency responses of the second-order differential-mode equivalent circuit in Fig. 1(b) associated to the proposed second-order balanced dual-band BPF. (a) Power transmission ($|S_{dd21}|$) and reflection ($|S_{dd11}|$) responses for differential-mode dual passbands with constant absolute bandwidth but with different center frequencies versus different values of the design impedances (Case 1: $Z_C = 42\Omega$, $Z_{0e1} = 77.5\Omega$, $Z_{0o1} = 31.8\Omega$, $Z_{0e2} = 98.7\Omega$, and $Z_{0o2} = 32.5\Omega$; Case 2: $Z_C = 20.4\Omega$, $Z_{0e1} = 79.4\Omega$, $Z_{0o1} = 24.9\Omega$, $Z_{0e2} = 117.23\Omega$, and $Z_{0o2} = 30.74\Omega$). (b) Power transmission ($|S_{dd21}|$) and reflection ($|S_{dd11}|$) responses for differential-mode dual passbands with different bandwidths versus different values of the design impedances (Case 1: $Z_C = 42\Omega$, $Z_{0e1} = 77.73\Omega$, $Z_{0o1} = 31.78\Omega$, $Z_{0e2} = 98.59\Omega$, and $Z_{0o2} = 32.6\Omega$; Case 2: $Z_C = 33\Omega$, $Z_{0e1} = 76.49\Omega$, $Z_{0o1} = 32.22\Omega$, $Z_{0e2} = 100.73\Omega$, and $Z_{0o2} = 31.03\Omega$).

realized. Additionally, the two passbands can be also designed with different bandwidths, but with fixed TZs at the frequency interval between these two passbands. As depicted in Fig. 3(b), the bandwidths of the dual passbands are enlarged from case 1 to case 2, where the TZs for the first passband at its left-hand side and for the second passband at the right-band side are shifted to lower and upper frequency locations, respectively, as a result of the referred bandwidth increase. In both cases, the two passbands are spectrally symmetrical with regard to the design frequency f_0. In addition, the common-mode power-rejection performance of the second-order balanced BPF versus different values of Z_L is also discussed. As depicted in Fig. 4, the common-mode suppression levels at the out-of-band spectral regions remain almost unchanged as Z_L is varied, whereas the power rejection levels within the frequency ranges of the differential-mode dual passbands are more sensitive to the employed low impedance Z_L. These results reveal that the value of Z_L should be properly chosen for the selected values of the line-impedance parameters of the differential-mode equivalent sub-circuit, which is vital to functionalize high common-mode suppression levels within the differential-mode dual passbands by means of common-mode multi-TZ creation. Consequently, the careful adjustment of the geometrical parameter associated to the impedance Z_L during the practical EM simulation becomes critical to attain high in-band common-mode rejection levels.

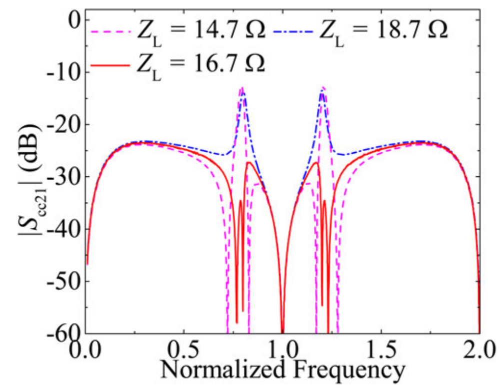

Fig. 4. Theoretical common-mode suppression ($|S_{cc21}|$) responses of the corresponding sub-circuit in Fig. 1(c) associated to the proposed second-order balanced dual-band BPF versus different values of Z_L when $Z_C = 42\Omega$, $Z_{0e1} = 77.5\Omega$, $Z_{0o1} = 31.8\Omega$, $Z_{0e2} = 98.7\Omega$, and $Z_{0o2} = 32.5\Omega$.

Finally, note that further flexibility may be attained by designing the coupled-line stages of the transversal filtering section as non-quarter-wavelength segments (i.e. $\theta_1(f_0)$, $\theta_2(f_0) \neq 90°$). In such case, spectrally-asymmetrical dual-band filtering transfer functions can be realized. This is demonstrated in Fig. 5, where two examples of differential-mode dual-passband responses with static in-band performance for the first passband and different bandwidth and center frequency for the second passband for each case are shown. Note that these two responses exhibit strong spectral asymmetry in terms of bandwidths and power-rejection profiles at their both sides, for which the design parameters of the transversal filtering section need to be properly adjusted. Nevertheless, more-complex common-mode suppression networks may be needed to attain high common-mode suppression levels in these situations, possibly involving the use of stepped-impedance-line segments and/or even more stubs connected at the symmetry plane of the overall circuit in Fig. 1(a).

Fourth-order balanced dual-band BPF

By exploiting the previously-proposed second-order balanced dual-band BPF as basic building block, its fourth-order balanced

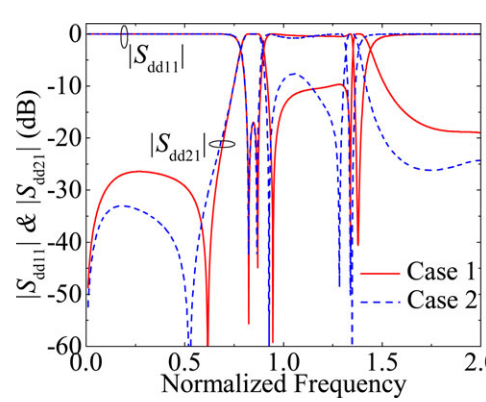

Fig. 5. Theoretical power transmission ($|S_{dd21}|$) and reflection ($|S_{dd11}|$) responses of the second-order differential-mode equivalent circuit in Fig. 1(b) for dual passbands with different bandwidths and out-of-band rejection profiles (Case 1: $Z_C = 42\Omega$, $Z_{0e1} = 77.73\Omega$, $Z_{0o1} = 31.78\Omega$, $Z_{0e2} = 98.59\Omega$, $Z_{0o2} = 32.6\Omega$, $\theta_1(f_0) = 77°$, and $\theta_2(f_0) = 84.5°$; Case 2: $Z_C = 26.3\Omega$, $Z_{0e1} = 76.27\Omega$, $Z_{0o1} = 32.72\Omega$, $Z_{0e2} = 84.8\Omega$, $Z_{0o2} = 32.82\Omega$, $\theta_1(f_0) = 79°$, and $\theta_2(f_0) = 85°$).

dual-band BPF counterpart can be developed. Such higher-order design is expected to show enhanced differential-mode passband selectivity and stopband power-attenuation levels, as well as increased in-band common-mode suppression levels. As depicted in Fig. 6(a), a fourth-order balanced dual-band BPF can be directly designed through two in-series-cascaded transversal coupled-line-based balanced dual-band BPF stages as the one detailed in Fig. 1. They are connected by means of half-wavelength-at-f_0 (i.e. electrical length $2\theta(f_0) = 180°$) line segments with characteristic impedance Z_{C1}. Consequently, the two-port differential- and common-mode equivalent sub-circuits of this proposed high-order balanced dual-band BPF topology are the ones provided in Figs 6(b) and 6(c), respectively, which are derived under applying the corresponding excitation at the pairs of input and output ports of the overall filter. To demonstrate the expected properties of this fourth-order balanced dual-band BPF architecture, its frequency responses compared with the ones of its constituent second-order balanced dual-band BPF in Fig. 1 are depicted in Fig. 7. As can be seen, highly-increased dual-passband filtering selectivity and augmented stopband power-rejection levels are attained with the selected values for the design impedances. Although two undesired spurious narrow-band peaks appear at the lower and upper stopband frequency regions under both differential- and common-mode excitations, they are attributed to the inter-stage cascading process as it was carefully analyzed in [23]. Furthermore, when compared to its building second-order balanced dual-band BPF stage, highly-enhanced common-mode power-suppression levels of this fourth-order balanced dual-band BPF design are obtained within the interval $[0.5f_0, 1.5f_0]$, which covers the operating frequency region of the differential-mode dual passbands. Note finally that this multi-stage in-series-cascaded design approach can be extended to any number of replicas for even higher-order balanced dual-band BPF realizations.

Digital modeling

As it can be seen in the theoretical design examples in Fig. 7, the ideally-synthesized power transmission responses of the proposed balanced dual-band BPFs are frequency periodic of period $2f_0$ for both the differential and common modes. This fact leads to the possibility of modeling these circuits as discrete-time linear time-invariant systems with a frequency response being periodic of period 2π rad/sample. Despite such framework was initially proposed

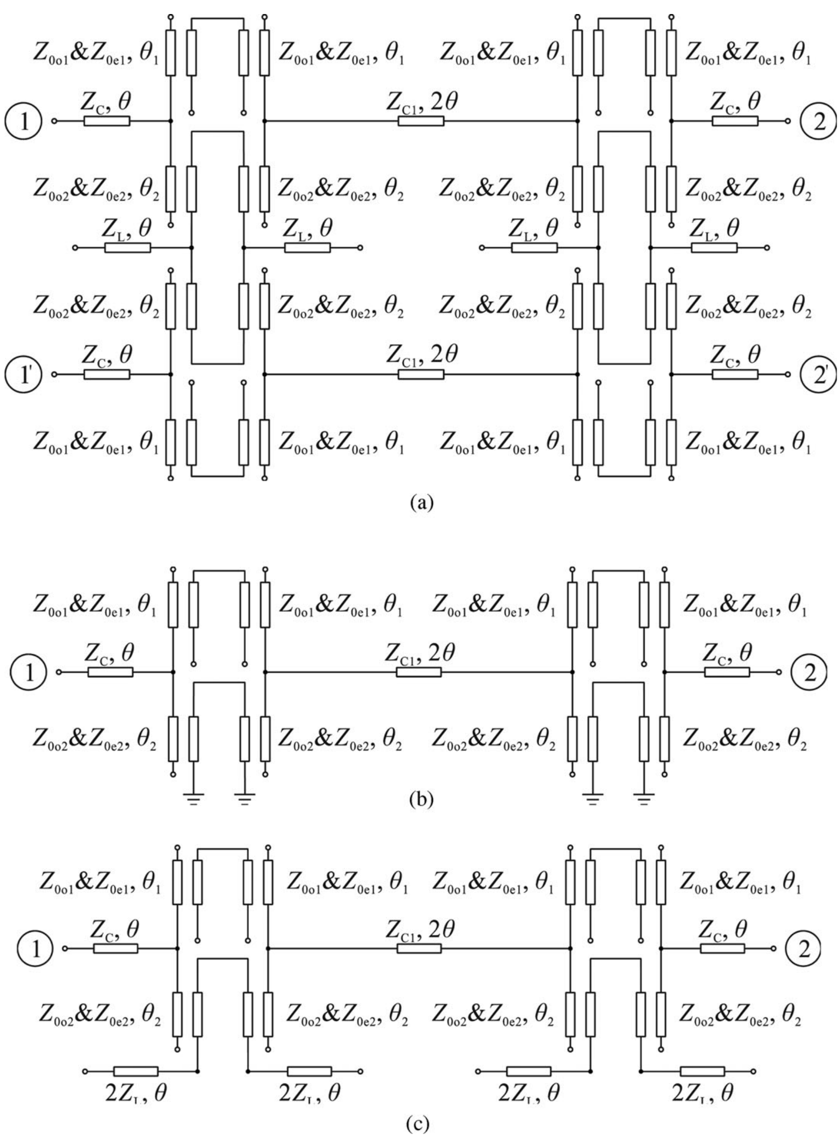

Fig. 6 - B/W online, B/W in print

Fig. 6. Equivalent circuits of the proposed fourth-order balanced dual-band BPF based on the connection of two replicas of the in-series cascaded second-order balanced transversal coupled-line-based dual-band BPF units in Fig. 1 through half-wavelength microstrip lines. (a) Four-port balanced dual-band BPF network. (b) Two-port differential-mode equivalent sub-circuit. (c) Two-port common-mode equivalent sub-circuit.

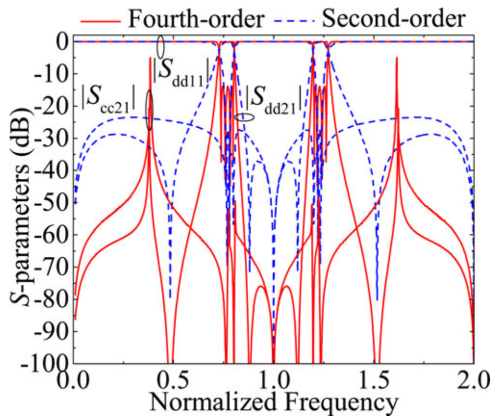

Fig. 7 - Colour online, B/W in print

Fig. 7. Theoretical differential-mode power transmission ($|S_{dd21}|$), reflection ($|S_{dd11}|$), and common-mode suppression ($|S_{cc21}|$) responses of the proposed fourth-order balanced dual-band BPF in Fig. 6 with $Z_C = 42\Omega$, $Z_{C1} = 50\Omega$, $Z_{0e1} = 77.5\Omega$, $Z_{0o1} = 31.8\Omega$, $Z_{0e2} = 98.7\Omega$, $Z_{0o2} = 32.5\Omega$, and $Z_L = 16.7\Omega$.

in [21] for signal-interference filters and extended to coupled-line filters in [22] of the single-ended type, its application to balanced/differential-mode RF filters has never been addressed. However, its conceptual interest is remarkable to properly understand the theoretical foundations of such balanced dual-band BPFs from a digital perspective, as well as to obtain discrete-time models for them which may be useful for their digital emulation. Thus, by applying this modeling method to frequency-periodic RF circuits containing coupled-line sections as the balanced dual-band BPFs of this work, the real-valued coefficients a_k ($k = 0, 1, \ldots, N$) and b_k ($k = 0, 1, \ldots, M$) of the transfer function of the digital system in the complex-valued variable z associated to the transmission scattering parameter of both the differential and common modes can be extracted.

As verification of the referred digital modeling, the coefficients a_k and b_k corresponding to the ideal design of the one-stage balanced dual-band BPF in Fig. 7 for the differential and common modes are listed in Tables 1 and 2, respectively. As observed, one interesting feature is that both sets of coefficients have identical orders $M = 6$ and $N = 8$ for both the differential and common modes. The zero-pole diagrams in the z-plane associated to the differential- and common-mode transmission scattering parameters for the one-stage circuit are drawn in Figs 8 and 9, respectively. Due to the passivity property of the circuit, the poles appear contained within the unit circumference. Moreover, the TZs are those located on the unit circumference. Finally, the two poles near the unit circumference in the second and third quadrants of the complex plane in Fig. 8 permit to explain the number of

Table 1. Coefficients a_k and b_k of the digital model associated to the differential-mode power transmission response of the one-stage balanced dual-band BPF in Fig. 7

k	a_k	b_k	k	a_k	b_k
0	1.0000	0.0343	5	−0.5034	−0.0603
1	2.3846	0.0603	6	0.0089	−0.0343
2	2.3690	0.0278	7	0.0533	–
3	0.5344	0.0000	8	0.0076	–
4	−0.6690	−0.0278	9	–	–

Table 2. Coefficients a_k and b_k of the digital model associated to the common-mode power transmission response of the one-stage balanced dual-band BPF in Fig. 7

k	a_k	b_k	k	a_k	b_k
0	1.0000	0.0343	5	−0.5456	−0.1066
1	2.6368	0.1066	6	0.0139	−0.0343
2	2.7239	0.1170	7	0.0552	–
3	0.6629	0.0000	8	0.0076	–
4	−0.7719	−0.1170	9	–	–

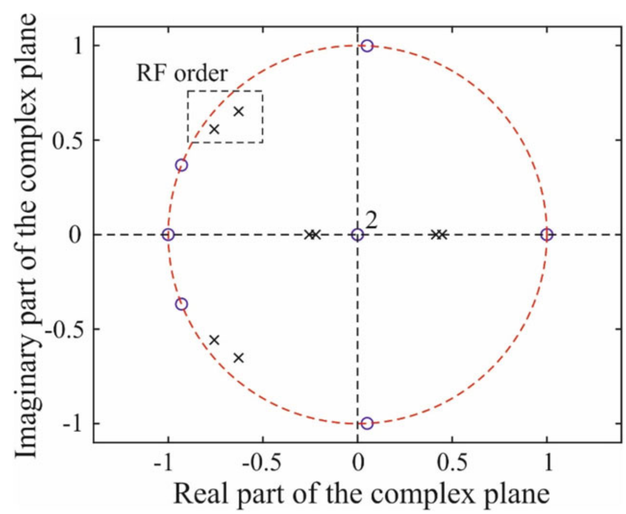

Fig. 8 - Colour online, B/W in print

Fig. 8. Zero-pole diagram of the digital system associated to the differential-mode transmission scattering parameter of the one-stage balanced dual-band BPF in Fig. 7 (poles are represented with black symbol “x”; zeros are represented with blue symbol “o”; numbers indicate the multiplicity of the root).

reflection zeros for each passband of the differential-mode power transmission parameter for this one-stage balanced dual-band BPF circuit (see Fig. 7).

The coefficients a_k and b_k corresponding to the ideal design of the two-stage balanced dual-band BPF in Fig. 7 for the differential and common modes are respectively listed in Tables 3 and 4, whereas the associated zero-pole diagrams are depicted in Figs 10 and 11, respectively. As can be seen, the polynomial orders are increased to $M = 10$ and $N = 14$, thus confirming the enhanced selectivity attained for the differential-mode passbands and the increased common-mode rejection levels for this two-stage design when compared to the one-stage balanced dual-band BPF. On the other hand, the number of poles near the unit circumference in the second and third quadrants of the complex plane in Fig. 10 are increased to four, which correctly matches with the observed number of reflection zeros for each passband of the differential-mode power transmission parameter for the two-stage balanced dual-band BPF design (see Fig. 7).

Implementation and measurement

To experimentally validate the high-order differential- and common-mode frequency responses in Fig. 7 (i.e. the selected design-parameter values were taken as starting point of the

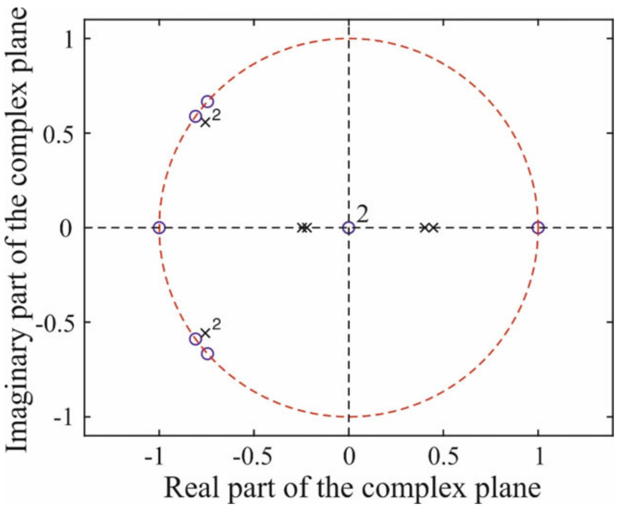

Fig. 9. Zero-pole diagram of the digital system associated to the common-mode transmission scattering parameter of the one-stage balanced dual-band TFS in Fig. 7 (poles are represented with black symbol "x"; zeros are represented with blue symbol "o"; numbers indicate the multiplicity of the root).

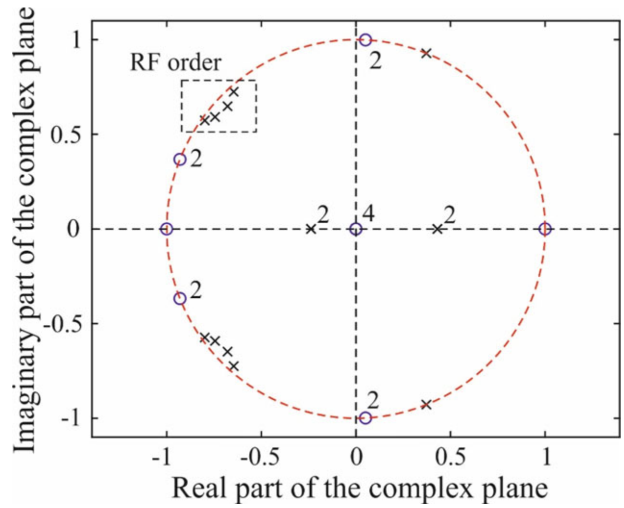

Fig. 10. Zero-pole diagram of the digital system associated to the differential-mode transmission scattering parameter of the two-stage balanced dual-band BPF in Fig. 7 (poles are represented with black symbol "x"; zeros are represented with blue symbol "o"; numbers indicate the multiplicity of the root).

Table 3. Coefficients a_k and b_k of the digital model associated to the differential-mode power transmission response of the two-stage balanced dual-band BPF in Fig. 7

k	a_k	b_k	k	a_k	b_k
0	1.0000	0.0011	8	0.3085	−0.0065
1	4.6026	0.0040	9	−2.2373	−0.0040
2	10.6267	0.0065	10	−1.5803	−0.0011
3	15.6807	0.0072	11	−0.3002	–
4	17.2254	0.0054	12	0.1506	–
5	15.5588	0.0000	13	0.0700	–
6	11.7286	−0.0054	14	0.0076	–
7	5.9216	−0.0072	15	–	–

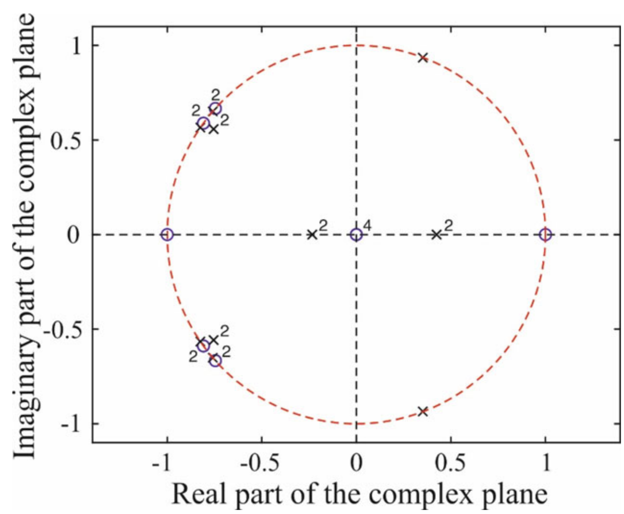

Fig. 11. Zero-pole diagram of the digital system associated to the common-mode transmission scattering parameter of the two-stage balanced dual-band BPF in Fig. 7 (poles are represented with black symbol "x"; zeros are represented with blue symbol "o"; numbers indicate the multiplicity of the root).

Table 4. Coefficients a_k and b_k of the digital model associated to the common-mode power transmission response of the two-stage balanced dual-band BPF in Fig. 7

k	a_k	b_k	k	a_k	b_k
0	1.0000	0.0011	8	0.3161	−0.0198
1	5.1006	0.0071	9	−2.7513	−0.0071
2	12.4948	0.0198	10	−1.8514	−0.0011
3	19.1703	0.0311	11	−0.2997	–
4	21.3885	0.0253	12	0.1757	–
5	19.4186	0.0000	13	0.0738	–
6	14.6340	−0.0253	14	0.0076	–
7	7.3779	−0.0311	15	–	–

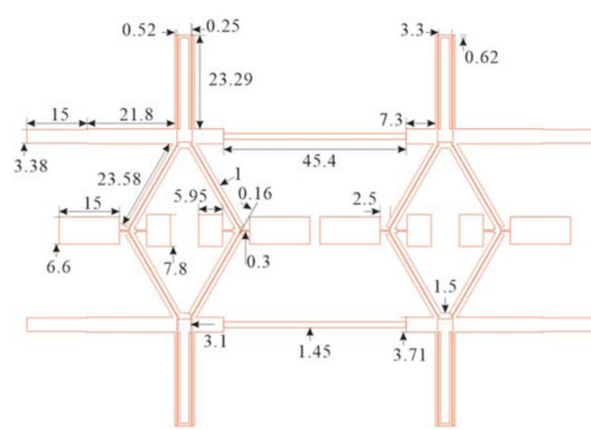

Fig. 12. Layout of the implemented fourth-order balanced dual-band BPF based on its relevant four-port equivalent circuit in Fig. 6 (all the indicated physical dimensions are given in mm).

layout-level design process), a planar fourth-order balanced dual-band BPF prototype is simulated and manufactured in microstrip technology. A Rogers 4003C substrate with relative dielectric constant $\epsilon_r = 3.55$, dielectric thickness $h = 1.524$ mm, metal thickness

Fig. 13 - Colour online, B/W in print

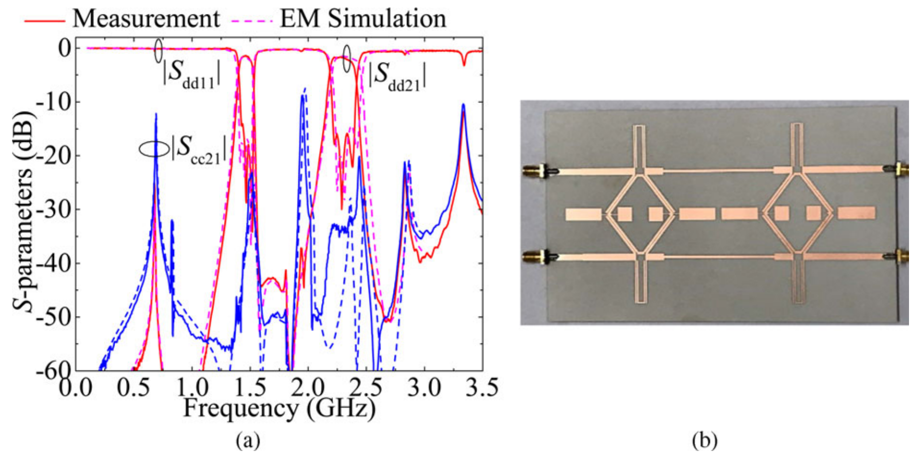

Fig. 13. Manufactured fourth-order balanced dual-band BPF prototype with its layout in Fig. 11. (a) Simulated and measured differential-mode power transmission ($|S_{dd21}|$), reflection ($|S_{dd11}|$), and common-mode suppression ($|S_{cc21}|$) responses. (b) Photograph.

Table 5. Comparison with other prior-art balanced dual-band BPFs

Ref.	CF (GHz)	Number of close-to passband TZs under DM	Order	3 dB FBW (%)	IL (dB)	In-band CM suppression
[3]	0.9/2.49	3	2	3.6/2.1	2.67/4.65	30 dB/40 dB
[4]	2.6/5.8	4	2	10.4/3.6	1.1/2.15	62 dB/48 dB
[6]	2.4/3.57	3	2	8/5.63	0.87/1.9	28 dB/31 dB
[7]	2.5/5.6	3	2	8/5	1.29/1.97	34.7 dB/24.1 dB
Figure 10 in [9]	1.98/2.5	3	2	5.37/5.85	2.17/1.71	59 dB/54 dB
Figure 11 in [9]	2.44/3.5	3	2	4.98/2.7	2.07/2.21	50 dB/47 dB
This work	1.464/2.294	5	4	8.74/9.68	1.396/1.61	23.16 dB/31.36 dB

CF, center frequency; DM, differential mode; FBW, fractional bandwidth; IL, insertion loss; CM, common mode.

$t = 35\,\mu$m, and dielectric loss tangent $\tan(\delta_D) = 0.0027$ is employed for its fabrication. Figure 12 depicts the layout of the proposed fourth-order balanced BPF. As it was previously discussed, in order to achieve high in-band common-mode power-rejection levels for the proposed second-order balanced dual-band BPF, low-impedance lines being loaded at the symmetry plane of the circuit are employed. However, considering the large line widths of the low-impedance microstrip lines, a low-impedance microstrip line connected by a section of high-impedance microstrip line, which results in an SIR-type structure, is utilized in the practical EM simulation of the proposed fourth-order balanced dual-band BPF. Specifically, in order to attain high in-band common-mode suppression levels, two pairs of the suggested SIR-type microstrip lines with different lengths are loaded at the filter symmetry plane as it can be visualized in the layout in Fig. 12. Note also that a fine optimization of the overall circuit was needed after the inclusion of such SIR-type stubs to obtain the expected results in terms of differential-mode sharp-rejection dual-passband filtering response with in-band common-mode suppression.

The EM-simulated and measured results of the manufactured fourth-order balanced dual-band BPF prototype, along with its photograph, are depicted in Fig. 13. The proposed fourth-order dual-band BPF is initially designed with center frequencies of 1.45 and 2.3 GHz, respectively. As shown in Fig. 13(a), a fairly-close agreement between the EM-simulated and measured results is attained. The measured differential-mode BPF features two quasi-elliptic-type sharp-rejection passbands with enhanced stopband-power-attenuation levels. On the other hand, for the EM simulated and measured common-mode suppression, the presence of some unexpected spurious narrow-band spikes at the spectral region between two differential-mode passbands is observed. Their origin is associated with the adopted physical layout for the filter prototype, mostly with the coupled-line-based sections that are connected by microstrip lines in small physical dimensions and the loaded SIR-type microstrip lines at the filter symmetry plane.

The main measured performance metrics of this engineered fourth-order differential-mode dual-band BPF for the lower and upper differential-mode passbands, respectively, are as follows: center frequencies of 1.464 and 2.294 GHz, minimum in-band insertion-loss levels of 1.396and 1.61 dB, minimum in-band return-loss levels of 14.13 and 15.86 dB, and 3 dB fractional bandwidths of 8.74 and 9.68%, respectively. In addition, the measured in-band common-mode rejection levels are higher than 23.16 and 31.36 dB for the measured balanced dual-band BPF. Furthermore, a performance comparison of the devised fourth-order balanced BPF prototype with other related prior-art balanced dual-band BPFs is given in Table 5. As can be seen, the fourth-order differential-mode dual-band BPF in this work features the highest order for the differential-mode passbands that provides it very-sharp-rejection capabilities, the highest number of TZs, and the widest fractional bandwidth for the second passband along with competitive in-band insertion loss. Furthermore, it is the only one exploiting the transversal-signal-interference filtering formalism, exhibiting in-band common-mode suppression levels that are comparable to those of some other previously-published related designs, such as those in [6] and [7].

Conclusion

A class of planar balanced transversal coupled-line-based dual-band BPFs with quasi-elliptic-type response has been reported. Based on the proposed second-order balanced dual-band BPF stage, its operational characteristics under differential- and common-mode excitations are detailed. To further improve the differential-mode passband selectivity and stopband attenuation levels of the second-order balanced dual-band BPF stage, as well as the in-band common-mode suppression levels, in-series-cascaded multi-stage designs particularized in a two-stage/fourth-order realization have been illustrated. Finally, a fourth-order balanced dual-band BPF microstrip prototype is designed, simulated, and characterized to validate the design concept. Although common-mode spurious peaks appear at the spectral region between the differential-mode dual passbands, very-sharp-rejection differential-mode passbands with TZs are measured, along with acceptable in-band common-mode suppression levels. As an additional contribution of this work, the digital modeling of these types of balanced dual-band BPFs has been shown, this being the first time it is applied to differential-mode RF filters.

Acknowledgements. This work was supported in part by the GOT ENERGY TALENT (GET) fellowship program cofunded by the EU as part of the H2020-MSCA-COFUND program under Grant Agreement number 754382 and in part by the Spanish Ministry of Economy, Industry, and Competitiveness (State Research Agency) under Project PID2020-116983RB-I00.

References

1. **Martin F, Zhu L, Hong J-S and Medina F** (2018) *Balanced Microwave Filters*, 1st Edn. New York, NY, USA: Wiley.
2. **Shi J and Xue Q** (2010) Novel balanced dual-band bandpass filter using coupled stepped-impedance resonators. *IEEE Microwave and Wireless Components Letters* **20**, 19–21.
3. **Yang L, Choi W-W, Tam K-W and Zhu L** (2015) Balanced dual-band bandpass filter with multiple transmission zeros using doubly short-ended resonator coupled line. *IEEE Transactions on Microwave Theory and Techniques* **63**, 2225–2232.
4. **Ren B, *et al.*** (2018) Compact dual-band differential bandpass filter using quadruple-mode stepped-impedance square ring loaded resonators. *IEEE Access* **6**, 21850–21858.
5. **Ren B, Guan X, Liu H, Ma Z and Ohira M** (2022) Highly selective and controllable superconducting dual-band differential filter with attractive common-mode rejection. *IEEE Transactions on Circuits and Systems II: Express Briefs* **69**, 939–943.
6. **Cho Y-H and Yun S-W** (2013) Design of balanced dual-band bandpass filters using asymmetrical coupled lines. *IEEE Transactions on Microwave Theory and Techniques* **61**, 2814–2820.
7. **Bagci F, Fernández-Prieto A, Lujambio A, Martel J, Bernal J and Medina F** (2017) Compact balanced dual-band bandpass filter based on modified coupled-embedded resonators. *IEEE Microwave and Wireless Components Letters* **27**, 31–33.
8. **Zhang S-X, Qiu L-L and Chu Q-X** (2017) Multiband balanced filters with controllable bandwidths based on slotline coupling feed. *IEEE Microwave and Wireless Components Letters* **27**, 974–976.
9. **Wei F, Yu JH, Zhang CY, Zeng C and Shi XW** (2020) Compact balanced dual-band BPFs based on short and open stub loaded resonators with wide common-mode suppression. *IEEE Transactions on Circuits and Systems II: Express Briefs* **67**, 3043–3047.
10. **Gómez-García R, Loeches-Sánchez R, Psychogiou D and Peroulis D** (2018) Multi-stub-loaded differential-mode planar multiband bandpass filters. *IEEE Transactions on Circuits and Systems II: Express Briefs* **65**, 271–275.
11. **Gómez-García R, Muñoz-Ferreras J-M, Feng W and Psychogiou D** (2018) Balanced symmetrical quasi-reflectionless single- and dual-band bandpass planar filters. *IEEE Microwave and Wireless Components Letters* **28**, 798–800.
12. **Gómez-García R, Sánchez-Renedo M, Jarry B, Lintignat J and Barelaud B** (2009) A class of microwave transversal signal-interference dual-passband planar filters. *IEEE Microwave and Wireless Components Letters* **19**, 158–160.
13. **Sánchez-Soriano MA, Bronchalo E and Torregrosa-Penalva G** (2009) Dual band bandpass filters based on strong coupling directional couplers. In *Proceedings of the 39th European Microwave Conference, Rome, Italy, Sep. 28–Oct. 2*, pp. 1401–1404.
14. **Gómez-García R and Sánchez-Renedo M** (2010) Microwave dual-band bandpass planar filters based on generalized branch-line hybrids. *IEEE Transactions on Microwave Theory and Techniques* **58**, 3760–3769.
15. **Gómez-García R, Muñoz-Ferreras J-M and Sánchez-Renedo M** (2011) Microwave transversal six-band bandpass planar filter for multi-standard wireless applications. In *Proceedings of the IEEE Radio Wireless Symposium, Phoenix, AZ, USA, Jan. 16–19*, pp. 166–169.
16. **Feng WJ and Che WQ** (2011) Ultra-wideband bandpass filter using broadband planar Marchand balun. *IET Electronics Letters* **47**, 198–199.
17. **Mirzaee M and Virdee S** (2013) UWB bandpass filter with notch-band based on transversal signal-interaction concepts. *IET Electronics Letters* **49**, 399–401.
18. **Gómez-García R and Yang L** (2021) Spurious-free signal-interference dual-band bandpass filters. In *Proceedings of the 2021 IEEE International Wireless Symposium, Nanjing, China, May 23–26*, pp. 1–3.
19. **Loeches-Sánchez R, Psychogiou D, Gómez-García R and Peroulis D** (2016) A class of differential-mode single/dual-band bandpass planar filters based on signal-interference techniques. In *Proceedings of the 2016 IEEE Wireless and Microwave Technology Conference, Clearwater Beach, FL, USA, Apr. 11–13*, pp. 1–6.
20. **Yang L, Malki M, Fan M and Gómez-García R** (2022) Transversal-coupled-line dual-band bandpass planar filters with quasi-elliptic-type response. In *Proceedings of 51st European Microwave Conference, London, United Kingdom, Apr. 2–7*, pp. 1–4.
21. **Muñoz-Ferreras J-M and Gómez-García R** (2014) A digital interpretation of frequency-periodic signal-interference microwave passive filters. *IEEE Transactions on Microwave Theory and Techniques* **62**, 2633–2640.
22. **Muñoz-Ferreras J-M, Psychogiou D and Gómez-García R** (2019) Digital modeling of microwave filters with coupled-line sections. In *Proceedings of the 2019 IEEE MTT-S International Conference on Numerical Electromagnetic Multiphysics Modeling and Optimization, Cambridge, MA, USA, May 29–31*, pp. 1–4.
23. **Morini A, Venanzoni G, Martín-Iglesias P, Ernst C, Sidiropoulus N, Donato AD and Farina M** (2018) Systematic evaluation of spikes due to interference between cascaded filters. *IEEE Transactions on Microwave Theory and Techniques* **66**, 4814–4819.

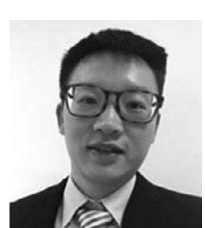

Photo. 01 - B/W online, B/W in print

Li Yang received the M.Sc. degree in electrical and electronics engineering and the Ph.D. degree in electrical and computer engineering from the University of Macau (UM), Macau, China, in 2013 and 2018, respectively. In 2018, he was a Research Associate with the Department of Electrical and Computer Engineering, UM. Since 2018, he holds a post-doctoral position with the Department of Signal Theory and Communications, University of Alcalá, Alcalá de Henares, Spain, where he is currently a GOT ENERGY TALENT (GET)-COFUND Marie Curie Fellow. His current research interests include

the synthesis and design of RF/microwave planar and multilayered passive filters, reconfigurable filters, filtering antennas, and multifunctional circuits and systems. Dr. Yang was a recipient of the Best Student Paper Award of the International Symposium on Antennas and Propagation 2010 in Macau.

Photo. 02 - B/W online, B/W in print

Mohamed Malki received the B.Sc. degree in telecommunication engineering from the University of Alcalá, Madrid, Spain, in 2020. He is currently pursuing the M.S. degree in telecommunication engineering, in the specialized area of Space and Defense Technologies at the University of Alcalá, Madrid, Spain. Since 2022, he joined the Department of Signal Theory and Communications at the University of Alcalá, Alcalá de Henares, Madrid, Spain, as a Research Assistant. His main research interests include the analysis, design, and construction of microwave filters and multiplexers.

Photo. 03 - B/W online, B/W in print

José-María Muñoz-Ferreras received the degree in telecommunication engineering and the Ph.D. degree in electrical and electronic engineering from the Polytechnic University of Madrid, Spain, in 2004 and 2008, respectively. He is currently an Associate Professor with the Department of Signal Theory and Communications, University of Alcalá, Alcalá de Henares, Spain. His current research interests include radar signal processing, advanced radar systems and concepts, and microwave/RF circuits and systems, specifically focusing on high-resolution inverse synthetic aperture radar images, and the design and validation of radar systems for short-range applications. Dr. Muñoz-Ferreras is a member of the IEEE MTT-S Biological Effects and Medical Applications (MTT-28) Technical Committee and a reviewer for several IEEE and IET publications. He serves as a member of the Technical Review Board of the IEEE International Geoscience and Remote Sensing Symposium, the IEEE Radar Conference, the European Radar Conference, and the IEEE MTT-S International Microwave Symposium.

Photo. 04 - B/W online, B/W in print

Roberto Gómez-García is a Full Professor with the Department of Signal Theory and Communications, University of Alcalá, Alcalá de Henares, Spain. His current research interests include the design of fixed/tunable high-frequency filters and multiplexers in planar, hybrid, and monolithic microwave-integrated circuit technologies, multifunction circuits and systems, and software-defined radio and radar architectures for telecommunications, remote sensing, and biomedical applications. In these topics, he has authored/co-authored about 125 papers in international journals and 165 papers in international conferences. He was a recipient of the 2016 IEEE Microwave Theory and Techniques Society (MTT-S) Outstanding Young Engineer Award. He is an IEEE Circuits and Systems Society Distinguished Lecturer (2020–2022). Besides, he is the Editor-in-Chief of IEEE Microwave and Wireless Components Letters (2022–2024). He has served and currently serve as Associate/Guest/Senior Editor for several *IEEE*, *IET*, and *EuMA* journals. He is also a member of several Technical Committees within MTT-S and CAS-S.